Original Research

Small-Scale Seismic Monitoring of Varying Water Levels in Granular Media

Sylvain Pasquet,* Ludovic Bodet, Paolo Bergamo, Roger Guérin, Roland Martin, Régis Mourgues, and Vincent Tournat

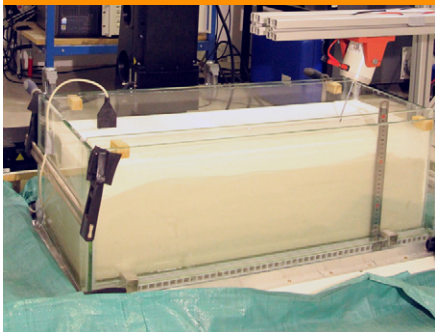### Core Ideas

- We tested the sensitivity of seismic measurements to water saturation variations.
- We used ultrasonic techniques to reproduce a small-scale seismic acquisition setup.
- Measurements were performed on glass bead layers with varying water levels.
- Results of 3D numerical modelling were used to validate data at the dry state.
- Data difference trends between the dry and wet models match with the water level.

S. Pasquet, Sorbonne Univ., UPMC Univ Paris 06, CNRS, EPHE, UMR 7619 METIS, 4 place Jussieu, 75005 Paris, France, and now at Wyoming Center for Environmental Hydrology and Geophysics and Dep. of Geology and Geophysics, Univ. of Wyoming, Laramie, WY 85071; L. Bodet and R. Guérin, Sorbonne Univ., UPMC Univ Paris 06, CNRS, EPHE, UMR 7619 METIS, 4 place Jussieu, 75005 Paris, France; P. Bergamo, School of Planning Architecture and Civil Engineering, Queen's Univ. Belfast, Belfast, UK; R. Martin, CNRS, Univ. Paul Sabatier, Observatoire Midi-Pyrénées, UMR 5563 GET, 31000 Toulouse, France; R. Mourgues, LUNAM Univ., Univ. du Maine, UMR 6112 LPG, 72000 Le Mans, France; and V. Tournat, LUNAM Univ., CNRS, Univ. du Maine, UMR 6613 LAUM, 72000 Le Mans, France. *Corresponding author (spasquet@uwyo.edu).

Physical properties of soils in the vadose zone, and especially their water content, are characterized by strong spatial and temporal variations mostly driven by weather and anthropogenic activities. To understand this variability and help water resource management, seismic methods have been recently suggested as a complement to electrical and electromagnetic techniques. The simultaneous in situ estimation of pressure (P) and shear (S) wave velocities (V_P and V_S, respectively) and their ratio (V_P/V_S) offers novel perspectives for the monitoring of space and time variations of vadose zone mechanical properties. However, the seismic response in partially saturated and unconsolidated soils remains complex and deserves to be studied both theoretically and experimentally. In this study, we tested the sensitivity of seismic measurements (i.e., P-wave travel times and surface-wave phase velocities) to water saturation variations using controlled physical models at the laboratory scale. Ultrasonic techniques were used to reproduce a small-scale seismic acquisition setup at the surface of glass bead layers with varying water levels. Travel times and phase velocity measurements obtained at the dry state were validated with both theoretical models and numerical simulations and serve as reference datasets. The increasing water level clearly affected the recorded wave field in both its phase and amplitude. In these cases, the collected data cannot yet be inverted in the absence of a comprehensive theoretical model for such partially saturated granular media. The differences in travel time and phase velocity observed between the dry and wet models show patterns that interestingly match the observed water level and depth of the capillary fringe, thus offering attractive perspectives for studying soil water content variations.

Abbreviations: GB, glass bead; SW, surface wave.

Increasing needs for fresh water in agricultural, industrial, and domestic activities require a thorough understanding of the various processes playing a part in the water cycle. More particularly, the vadose zone (i.e., the unsaturated area connecting the atmosphere to groundwater reservoirs) is of great importance in this cycle because it governs plants' access to water and acts as a buffer protecting the groundwater from surface pollutants. The physical properties of the soils present in the vadose zone, and especially their water content, are characterized by strong spatial and temporal variations mostly driven by weather and anthropogenic activities.

To understand this variability and help with water resource management, scientists seek to measure and monitor the soil water content at different scales using a large variety of techniques. At the regional scale (>10 km^2), remote sensing is extensively used to estimate the soil moisture distribution across large areas (Ines and Mohanty, 2008, 2009; Vereecken et al., 2012). However, remote sensing techniques allow for characterizing only the very shallow layers of the soil (<10 cm for frequencies >1.5 GHz) (Njoku and Entekhabi, 1996) and thus cannot investigate the entire thickness of the vadose zone. At the field scale ($\sim$1 dm^2), measurements are performed at several points thanks to in situ

sensors such as temperature or time domain reflectometry (TDR) probes. Temperature measurements can be made to monitor water fluxes through the soil thanks to convective and conductive heat transfer models (Cheviron et al., 2005; Read et al., 2013; Bechkit et al., 2014). The TDR method provides a reliable tool for soil water content estimation due to the high dielectric permittivity contrast between water and soil constituents (Topp et al., 1980, 1988; Robinson et al., 2003). When networked with a multiplexer, TDR probes can measure the soil water content at different depths ranging from tens of centimeters to several meters (Takagi and Lin, 2011). However, the destructive nature of such a setup and its spatial scarcity prevent it from being used at the catchment scale (0.1–1 km^2). At this intermediate scale, near-surface geophysical techniques such as ground-penetrating radar (Huisman et al., 2003), electrical resistivity tomography (Amidu and Dunbar, 2007; Cassiani et al., 2012; Garré et al., 2011, 2013), or electromagnetic induction (Reedy and Scanlon, 2003; Martini et al., 2015) have been increasingly used in the last decade. They are particularly well suited for the characterization of near surface physical properties at the catchment scale because they provide nondestructive measurements across large areas, with high investigation depth and fine resolution (Binley et al., 2015; Parsekian et al., 2015). In all cases, soil moisture is estimated indirectly using various empirical and physical laws developed to describe the measured parameter (e.g., electrical resistivity, dielectric permittivity) as a function of soil water content (Robinson et al., 2008).

If electrical and electromagnetic methods have shown their efficiency in a large range of applications, they can occasionally be ineffective in electrically conductive media such as fine-textured soils (e.g., loess, clays). Under these conditions, a high-frequency electromagnetic signal can be greatly attenuated, thus limiting the depth of investigation of geophysical techniques such as ground penetrating radar. Furthermore, the integrative properties of electrical and low-frequency electromagnetic methods can prevent precise delineation of the studied structures. To overcome these limitations, seismic methods have been recently proposed for the monitoring of seasonal (Lu, 2014; Pasquet et al., 2015a; Bergamo et al., 2016) and spatial (Konstantaki et al., 2013; Pasquet et al., 2015b) variations of the near-surface mechanical properties linked to water content. A specific methodology has been developed for the joint study of pressure- and shear-wave seismic velocities (V_P and V_S, respectively), whose evolution is strongly decoupled in the presence of fluid (Biot, 1956a, 1956b). The estimation of V_P/V_S space and time variations provided results in good agreement with a priori geological information and existing geophysical and piezometric data. More particularly, Pasquet et al. (2015a) highlighted an interesting consistency between strong contrasts of V_P/V_S and variations in the gravimetric water content measured in auger soundings samples. Yet an incompatibility persists between these two observables because V_P/V_S is estimated through a layered interpretation, whereas the water content clearly shows a continuously varying trend. This calls into question the pertinence of the

layered direct models used to estimate V_P/V_S in such continuous media and shows a need to improve inversion and interpretation techniques through advanced experimental developments in more controlled media.

Laboratory physical modeling is frequently proposed with non-contact ultrasonic techniques to study seismic wave propagation at various scales, with a wide range of applications in civil engineering (Ruiz and Nagy, 2004; Lu et al., 2011; Abraham et al., 2012), near-surface geophysics (Bodet et al., 2005, 2009; Bretaudeau et al., 2011; Bergamo et al., 2014), exploration seismic (Campman et al., 2004, 2005; de Cacqueray et al., 2011, 2013), or seismology (Nishizawa et al., 1997; van Wijk and Levshin, 2004). The non-contact character of ultrasonic techniques and their high-density sampling abilities provide flexibility that gives the opportunity to reproduce typical seismic records in the laboratory. In most of the studies cited above, small-scale seismograms were recorded at the surface of physical models (with dimensions around several decimeters) specifically designed to benchmark processing or inversion techniques, using a mechanical source and a laser-Doppler vibrometer. Bodet et al. (2014) recently showed that it was possible to build physical models with unconsolidated granular materials such as natural sands or glass beads (GBs), which are well-characterized in terms of elastic parameters (Jacob et al., 2008; Bodet et al., 2010). They showed that pressure-wave (P-wave) first arrival times and surface-wave (SW) dispersion could be extracted from these seismograms and inverted for one-dimensional P- and shear-wave (S-wave) propagation velocity profiles with depth. In addition, granular media offer an obvious flexibility in terms of model geometry and choice of mechanical parameters (Bergamo et al., 2014), thus allowing seismic-wave propagation through physical models of increasing degrees of complexity to be addressed. In a recent study, Bodet et al. (2012) were, for instance, able to record small-scale seismograms at the surface of granular models with controlled porosity and permeability and varying pore overpressure.

In the present study, we faced the challenge of applying the same approach on fully and partially saturated media to test the sensitivity of seismic methods to water saturation. We had to adapt the laboratory setup developed by Bodet et al. (2010, 2014) to meet experimental requirements in terms of boundary wall impermeability and rigidity, while keeping the size and weight of the entire setup to a practical level. We built a glass tank with reduced dimensions (800 by 400 by 300 mm) compared with the box used by Bodet et al. (2010, 2014) in their previous experiments (1000 by 800 by 300 mm), with two side reservoirs aimed at imbibing the granular medium from the bottom. At first, we filled the tank with dry GBs and recorded small-scale seismic lines at the surface of the medium using the same mechanical source and laser-Doppler vibrometer. However, strong noise originating from conversion and backscattering at the interface between GBs and the glass walls prevented the identification of SW dispersion curves in a straightforward manner. These curves were eventually identified

and picked along with P-wave first arrival times after muting the recorded seismogram to remove most of the noise. The recorded seismograms were compared with synthetic seismograms obtained with elastic three-dimensional finite difference simulations to assess the effects of this processing technique and validate the extracted P-wave first arrival times and SW dispersion curves. These data were then inverted to retrieve one-dimensional P- and S-wave propagation velocity profiles with depth, which offered a good match with previously estimated properties of the probed medium (Bodet et al., 2010, 2014). The water level was then gradually increased in the granular medium so as to perform two distinct acquisitions with two different water levels. The data obtained with the dry model and with the two different water levels were finally compared to estimate the thicknesses of the fully, partially, and unsaturated areas of the granular medium. Before describing these experiments and the results associated with varying water levels, we provide below a brief presentation of the theoretical background related to elasticity of unconsolidated granular media and how they are probed.

◆ Acoustic Probing and Wave Propagation in Unconsolidated Granular Media

The elastic properties of an unconsolidated granular packed structure under gravity can be described with the Hertz–Mindlin contact theory to model the intergrain forces. In the mechanically free-surface vicinity of such a medium, the P- and S-wave propagation velocity ($V_{P,S}$) can be considered as being power-law dependent on pressure (Gassmann, 1951):

$$V_{P,S} = \gamma_{P,S} (\sigma)^{\alpha_{P,S}} \qquad [1]$$

where $\gamma_{P,S}$ is a coefficient depending mainly of the elastic properties of the grains and the porosity and coordination number of the packed structure, σ is the stress, and $\alpha_{P,S}$ is the power-law exponent predicted equal to 1/6 when considering a random close packing of uniform spheres. In a homogeneous medium, the bulk density (ρ) can be assumed constant, and the stress σ thus corresponds to the isostatic pressure $p = \rho g z$, with g being the gravity acceleration and z the depth. Laboratory experiments have shown that within real materials, several imperfections such as weak dispersion in grain sizes or sphericity can lead to strong contact disorders, which may induce deviations of $\alpha_{P,S}$ from 1/6 (Makse et al., 2004; Zimmer et al., 2007; Tournat and Gusev, 2010). More recently, Jacob et al. (2008) and Bonneau et al. (2008) experimentally observed coefficients close to 1/3 at very low pressure, typically <1 kPa, going down to <100 Pa (Tournat and Gusev, 2010).

While most of these experiments were performed on material samples confined at a given pressure in a cell, Jacob et al. (2008) and Bodet et al. (2010, 2014) proposed to estimate $\alpha_{P,S}$ at very

low pressures from seismograms recorded at the surface of an unconfined granular media using a laser-Doppler vibrometer and a mechanical source. They interpreted the first arrivals and dispersive wave train identified on the small-scale seismograms as typical seismic events. Assuming a P-wave train of weak dispersion at high frequencies, first-arrival times were picked as P-wave travel times. As for dispersive events, the recorded wave field was transformed into the frequency–wavenumber domain, where maxima are approximated as different propagation modes of the SW (for a more detailed description of those aspects, see Bodet et al., 2014). Considering the medium as a succession of thin layers with continuously increasing velocities (Bachrach et al., 1998, 2000), travel-time and dispersion data were finally inverted in the framework of elastic wave propagation in stratified media to infer one-dimensional V_P and V_S profiles defined by the coefficients $\gamma_{P,S}$ and $\alpha_{P,S}$.

When the water content increases in a porous medium, the stress σ in Eq. [1] no longer solely depends on gravity but also on pore pressure and capillary action (Bear, 1972; Cho and Santamarina, 2001; Lu and Likos, 2004). This so-called "effective stress" has been studied in many studies offering a wide variety of formulations, allowing for its calculation in unsaturated granular media (e.g., Terzaghi, 1936; Bishop, 1959; Fredlund et al., 1978; Fredlund and Rahardjo, 1993; Toker et al., 2014). Moreover, although studies have shown that V_P decreased slightly to 99% saturation and increased drastically beyond (Bachrach and Nur, 1998), others have suggested that very small changes in saturation (e.g., related to air humidity variations) may increase the cohesiveness of the granular medium (and therefore V_P) by creating "liquid bridges" between the beads (Bocquet et al., 1998; Soulié, 2005; Vandewalle et al., 2012). Similarly, if the increase in the density of the equivalent medium in the presence of water can lead to a small decrease in V_S, capillary forces observed at low saturation values are likely to have the opposite effect. Furthermore, Brunet et al. (2008) have shown, using ultrasonic probing with multiple scattered waves, that the acoustic absorption in GB packings is larger for wet samples than for dry ones. Although these experiments were performed for static pressures (>100 kPa) several orders of magnitude larger than in the present case, and for much higher wave frequencies (~500 kHz), the same trend can be expected here with an increase in wave attenuation in wet models compared with the dry one.

Following a similar methodology, P-wave first arrival times and SW dispersion data were thus extracted and inverted to estimate V_P and V_S models in the dry medium. Then to overcome the absence of a theoretical model able to compute travel times and dispersion data in partially saturated granular media, we proposed to exploit the data recorded on wet models by studying their sensitivity to the presence of water and interpret them in terms of depth of the water level and thickness of the capillary fringe.

● Experimental Setup and Data Acquisition

For this study, we built a glass tank with dimensions 800 by 400 by 300 mm, with two 50-mm-wide reservoirs installed lengthwise on both sides of the tank (Fig. 1a). These two reservoirs are connected with the central part by two 15-mm-high openings located at the tank bottom and covered with a metal sieve allowing imbibition of the granular medium from the bottom by gradually increasing the water level in the reservoirs. The length and width of the central portion of the tank were determined to record a seismic profile across a total length of 500 mm while keeping a minimum distance of 150 mm with the side walls.

Glass beads with a diameter of 1000 μm were used to build the physical model (PM1). Deposition of the beads was performed to ensure a homogeneous compaction of the medium. Ideally, pluviation systems such as those developed for geological (Maillot, 2013) or geotechnical (Murillo et al., 2009) modeling should be used to ensure an even distribution of GBs. However, the low cohesiveness of GBs and their well-classified size allow a homogeneous deposition without using this type of automatic equipment (Bodet et al., 2014). The GBs were therefore evenly distributed throughout a thickness of 255 mm by simply pouring them into a sieve following a rotary movement sweeping all the tank.

Based on the work of Bodet et al. (2014), the density of GBs could be approximated as 1600 kg m^{-3}. Similarly, Bodet et al. (2012) measured the permeability values of GBs with a similar granulometry (around 5000×10^{-12} m^2). The use of such GBs thus ensured a homogeneous imbibition of the model from the bottom. For each acquisition, the water level (z_{wat}, i.e., the depth of the water in the side reservoirs) and the capillary fringe (z_{cap}, i.e., the depth of the top of the capillary fringe above the water level) were ultimately increased stepwise by filling the side reservoirs. In this study, we performed three acquisitions, at first with the dry model (PM1-D, Fig. 1a) then with two distinct water levels (PM1-W1 with z_{wat} = 145 mm and z_{cap} = 100 mm, Fig. 1b; and PM1-W2 with z_{wat} = 85 mm and z_{cap} = 50 mm, Fig. 1c). The water level and the height of the
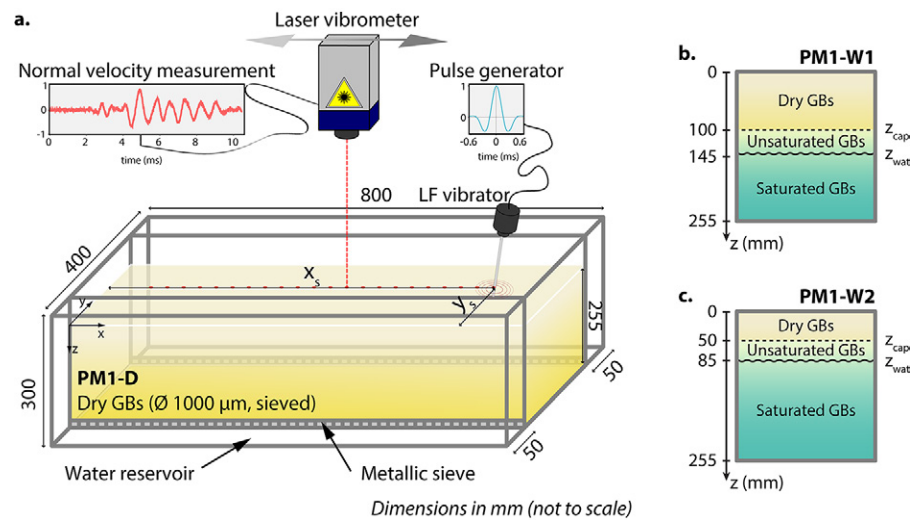

Fig. 1. (a) Sketch of the experimental setup used to prepare physical models and record seismograms at the surface of the medium. The model PM1-D was prepared with dry, 1000-μm-diameter glass beads (GBs) sieved into the central part the tank. The water level (z_{wat}) and the capillary fringe (z_{cap}) were then increased stepwise to obtain two distinct models: (b) PM1-W1 with z_{wat} = 145 mm and z_{cap} = 100 mm and (c) PM1-W2 with z_{wat} = 85 mm and z_{cap} = 50 mm.

capillary fringe were both estimated visually through the glass walls of the tank.

The acquisition setup presented in Fig. 1a involved a laser-Doppler vibrometer allowing the recording of the vertical particle displacement velocities at the surface of the granular medium excited by a mechanical source positioned at (x_s, y_s). In this study, the medium was mechanically excited by a 3-mm-diameter metal stick attached to a low-frequency vibrator driven by a waveform generator (Fig. 2a). The stick was buried in the granular material at an angle of 20° from normal to the free surface. The force source signal was a Ricker pulse with its frequency spectrum centered on 1.5 kHz (blue line in Fig. 2b). Except for a slight shift toward low
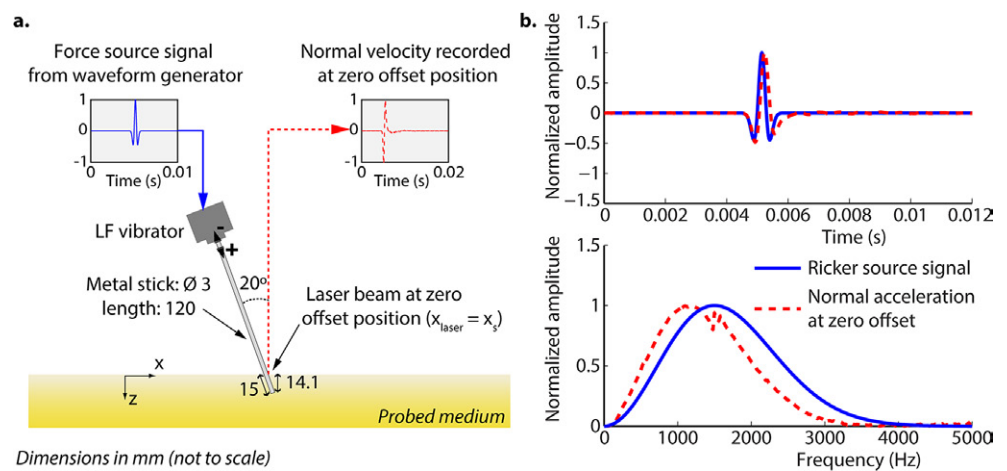

Fig. 2. (a) Sketch of the source used to generate the seismic signal in the granular medium. The force source signal is represented with a blue line on the left inset, while the stick normal velocity recorded at the zero offset position is represented with the dashed red line on the right inset; and (b) the shape of the Ricker pulse used as the force source signal (blue line) and differentiated signal recorded at the zero offset position (red dashed line) in the time domain (upper inset) and in the frequency domain (lower inset).

frequencies, probably due to the "ringing of the stick," the signal recorded at zero offset position (red dashed lines in Fig. 2b), differentiated to acceleration here, is in very good agreement with the original force source signal (blue lines in Fig. 2b). The force source signal has a very large bandwidth, with significant energy across the range 250 to 2750 Hz, while the vibrometer sensor head and the controller used to record the signal allow broadband acquisition (typically between 0.5 Hz and 1.5 MHz using an analog universal decoder). Maintaining the source at the same position (x_s = 655 mm; y_s = 150 mm), the surface of the medium was scanned by the laser with a constant step (Δx = 5 mm). One hundred traces were recorded with an oscilloscope along a profile oriented in the direction O_x (parallel to the length of the tank and at the center of its width), so as to retrieve 500-mm-long profiles. For each trace, 50 stacks were performed with a sampling rate of 100 kHz over 5002 points. For a single source position, the wave field was thus recorded as a "seismogram" representing the vertical component of the particle motion velocity at the surface of the granular medium.

Seismic Monitoring of the Granular Medium

Dry Model Characterization

Data Recorded on the Dry Model

The seismogram presented in Fig. 3a was obtained with the dry model PM1-D. Despite possible multiples due to ringing of the stick (Sr), the seismogram presents similar and coherent wave fields in which both P-wave and SW wave trains clearly appear. Hyperbola corresponding to bottom reflections (rP) are clearly identified as well. Energetic events with very low frequencies and low apparent velocities (C) are also visible at different times, masking part of the signal contained in the SW wave train. These events probably originated from the conversion and backscattering of guided waves at the interface between the granular medium and the glass walls of the tank.

This seismogram was then muted to keep only the SW wave field and reduce the influence of the converted waves (C in Fig. 3a). The mute operation consists of zeroing a part of the samples of one or several traces considered as noise. In this study, the mute limits were defined thanks to numerical modeling results (see the appendix). All the samples located outside the blue contour in Fig. 3a were progressively zeroed with a tapering function so as to minimize the appearance of Gibbs effects during the wave-field transform. A dispersion image was finally extracted from the muted seismogram using a slant stack in the frequency domain (Russel, 1987; Mokhtar et al., 1988). Figure 3b presents clear maxima (white error bars) that correspond to different propagation modes: (i) two SW modes at low frequency and low phase velocity between 0.25 and 1.25 kHz, noted 0 and 1; and (ii) one P mode at higher frequencies and velocities between 1.25 and 3 kHz.
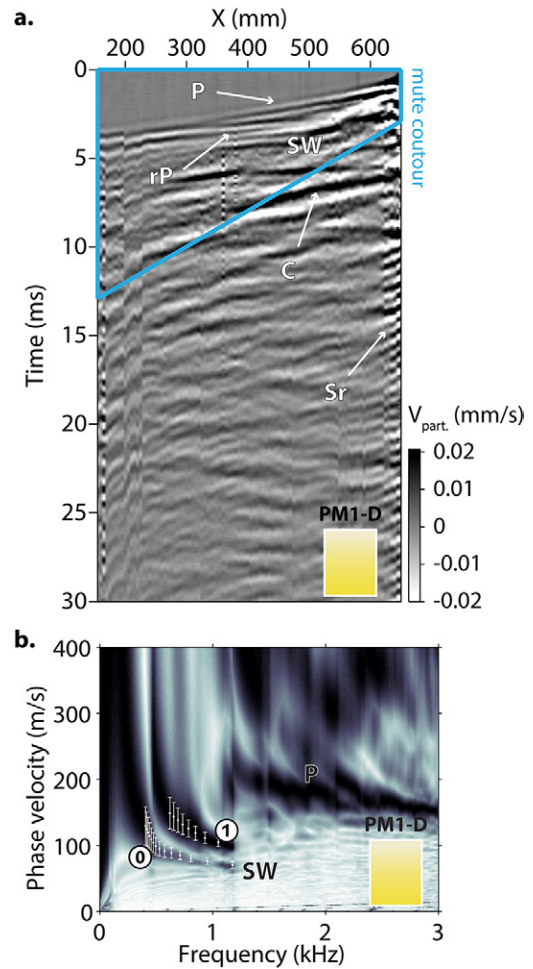

Fig. 3. (a) Seismogram representing the vertical component of the particle velocity, recorded at the surface of the dry model PM1-D. The recorded wave field presents coherent P and SW events. Strong bottom reflections are visible (rP), along with low-frequency energetic events (C). Strong amplitudes associated with source ringing (Sr) are also present at short offset. The blue contour corresponds to the limits of the mute applied prior to the extraction of the dispersion image; (b) normalized dispersion image obtained after transforming the muted wave field in the frequency–phase velocity domain thanks to a slant stack. The P and SW propagation modes are confirmed (maxima in black, with 0 and 1 being the SW fundamental and first higher modes, respectively). The picked dispersion curves are represented with white error bars.

Estimation of the Velocity Profiles

First arrival times were picked for each trace of the recorded seismogram (black crosses in Fig. 4a). They show a nonlinear increase of the travel time with the offset, which corresponds well to a velocity gravity gradient in depth. Following the methodology proposed by Bodet et al. (2010, 2014), we were able to invert first arrival times for a one-dimensional model of V_P in the dry granular medium. The best V_P model (red dashed line) is represented within a ±5% error (red solid lines) in Fig. 4b, along with the corresponding depth of investigation (DOI, black dashed line) estimated by retrieving the maximum propagation depth of the ray emerging at the last picked trace. The model is characterized by values of γ_P = 21.25 and α_P = 0.33. These values are slightly shifted compared with those observed by Jacob et
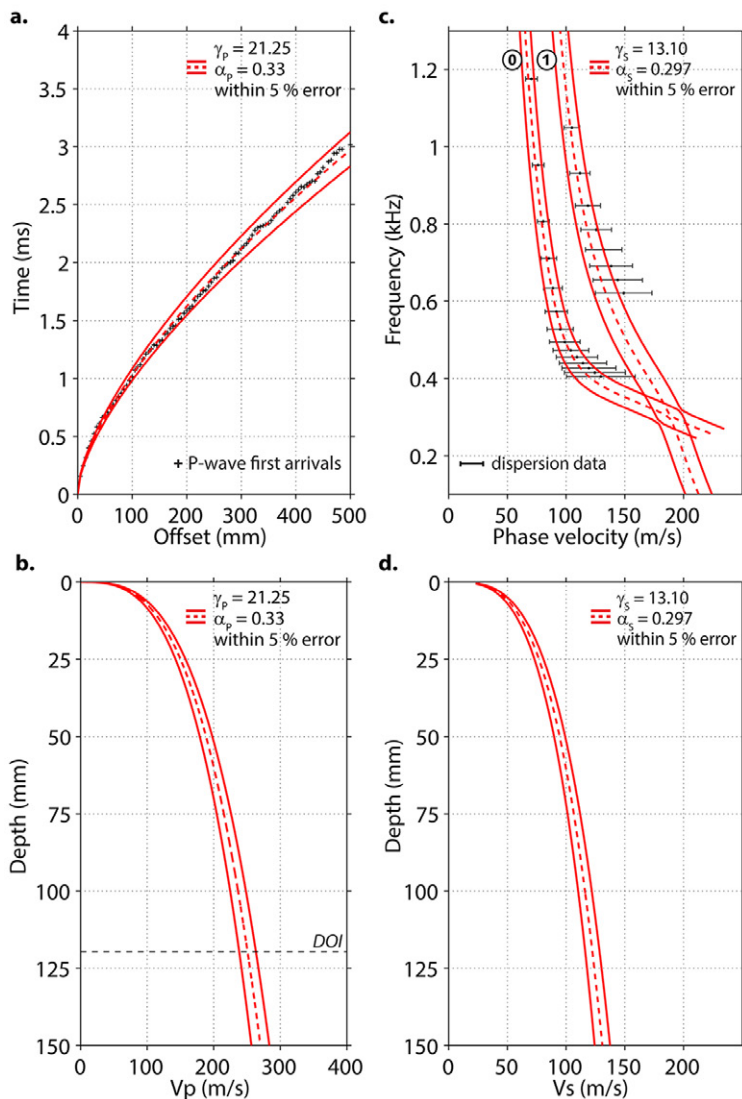
Fig. 4. (a) Pressure (P)-wave first arrival times picked at each trace of the seismogram in Fig. 3a (black crosses), with the calculated travel times corresponding to the best model obtained after inversion (red dashed line) represented within a ±5% error (red solid line); (b) P-wave velocity model corresponding to the best set of parameters obtained after travel-time inversion (red dashed line), represented within a ±5% error (red solid line), with the estimated depth of investigation (DOI) represented by the black dashed line; (c) dispersion data picked from the dispersion image in Fig. 3b for both fundamental (0) and first higher (1) propagation modes (black error bars), with the calculated dispersion curves corresponding to the final model obtained after inversion (red dashed line) represented within a ±5% error (red solid line); and (d) shear (S)-wave velocity model corresponding to the final set of parameters obtained after dispersion inversion (red dashed line), represented within a ±5% error (red solid line).

al. (2008) and Bodet et al. (2010, 2014), but the α_P value remains close to 1/3, as experimentally observed by Bonneau et al. (2008) and Jacob et al. (2008). Finally, the travel times calculated with the best V_P model are represented within a ±5% error to check the quality of the fit between observed and calculated travel times (Fig. 4a).

The SW fundamental (0) and first higher (1) modes were then picked in the extracted dispersion image with an estimated standard

error in phase velocity (black error bars in Fig. 4c) defined according to the workflow described by O'Neill (2003). Following the recommendations of Bodet et al. (2005, 2009) and O'Neill (2003), dispersion curves were limited to wavelengths close to 50% of the array length to mitigate near-field effects and prevent velocity underestimation at low frequency. As proposed by Bodet et al. (2010, 2014), we were also able to invert dispersion curves for a one-dimensional model of V_S. The final V_S model (red dashed line) is characterized by γ_S = 13.10, α_S = 0.297 and is represented within a ±5% error (red solid lines) in Fig. 4d. Again, the estimated power-law exponent correlates well with the observations made by Jacob et al. (2008) and Bodet et al. (2010, 2014) for S-wave velocity models. Theoretical dispersion curves computed with the final V_S model are finally represented within a ±5% error to verify the fit quality between observed and calculated phase velocities (Fig. 4c).

Wet Models Characterization
Data Recorded on the Wet Models
Seismograms obtained with different water levels are represented in Fig. 5a (PM1-W1 with z_{cap} = 100 mm) and Fig. 5c (PM1-W2 with z_{cap} = 50 mm). They both present a clear increase in the attenuation compared with the seismogram recorded on the dry model PM1-D (Fig. 3a), which is in agreement with the observations of Brunet et al. (2008). Pressure-wave events are visible on both seismograms but become hard to identify and pick at far offset for PM1-W2. These events are followed by the low-frequency SW wave field, hardly visible on PM1-W2. The bottom reflection hyperbola (rP) and the low-frequency energetic events (C) observed on the dry model can also be clearly identified for PM1-W1. Furthermore, the recorded wave field remains perturbed at short offset by the ringing of the source (Sr) for both wet models.

After muting the seismograms according to the blue contours in Fig. 5a and 5c, the corresponding dispersion images were extracted for PM1-W1 (Fig. 5b) and PM1-W2 (Fig. 5d). The maxima observed on these dispersion images allow the identification of the propagation modes present on the seismograms (white error bars). Three SW modes (noted 0–2) are visible at low frequency and low velocity for PM1-W1, along with a P mode characterized by higher frequencies and velocities, slightly faster than the P mode observed for the dry model (Fig. 3b). For PM1-W2, up to four SW modes are visible (noted 0–3), whereas the P mode is probably too fast to be observed.

Time-lapse Interpretation of Extracted Data
First arrival times were picked for each trace of both wet model seismograms PM1-W1 (cyan in Fig. 6a) and PM1-W2 (magenta in Fig. 6a). The results show a decrease of first arrival times for these partially saturated models compared with the dry model PM1-D

(black in Fig. 6a). The nonlinear increase in first arrival times with the offset related to the velocity gradient in depth remains visible for PM1-W1, while PM1-W2 shows first arrival times divided along three segments with distinct slopes. As for SW dispersion curves, both the fundamental and first higher modes show an overall trend of increasing phase velocities for PM1-W2 (magenta in Fig. 6b) relative to PM1-D (black in Fig. 6b), while PM1-W1 (cyan in Fig. 6b) shows an identical first higher mode and a decrease in phase velocity for the fundamental mode at frequencies <0.5 kHz.

Time differences were then calculated between the experimental first arrival times obtained for the reference dry model and those obtained for the partially saturated models. Time differences were evaluated locally with a moving window sliding along the offset axis, negative

differences referring to shorter travel times in the corresponding wet model. Using the elastic parameters estimated in the dry model, we were able to convert offset values in terms of pseudo-depth by retrieving the maximum propagation depth of theoretical rays emerging at each picked trace. The same approach was also applied for the dispersion data, using phase velocity vs. frequency curves of the fundamental mode. Indeed, the "simple" behavior of the fundamental mode allows the interpretation of dispersion curves in terms of velocity variations with depth as a first approximation. Phase velocity differences were estimated using a moving window sliding along the frequency axis, negative differences referring to slower phase velocities in the corresponding wet model. Finally, frequencies were transformed into wavelengths λ, which were then converted in pseudo-depths z using the approximation $z = 0.63\lambda$ proposed by Xia et al. (1999).
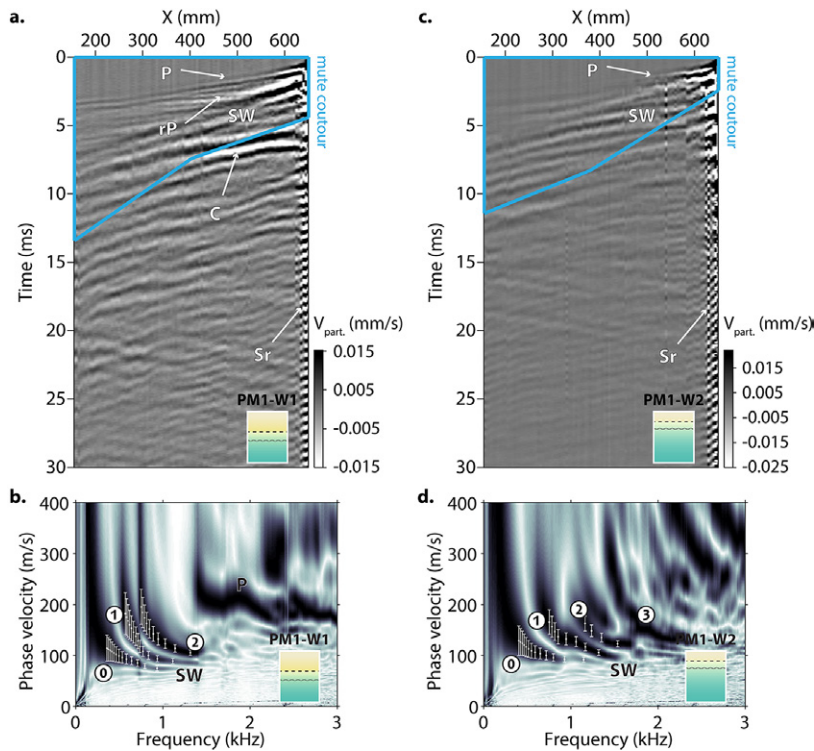

Fig. 5. (a) Seismogram recorded at the surface of the wet model PM1-W1; (b) normalized dispersion image extracted from the muted seismogram obtained for PM1-W1; (c) seismogram recorded at the surface of the wet model PM1-W2; and (d) normalized dispersion image extracted from the muted seismogram obtained for PM1-W2. The blue contours in (a) and (c) correspond to the limits of the mute applied prior to the extraction of the dispersion images. The recorded wave fields in (a) and (c) present coherent P and SW events. Strong amplitudes associated with source ringing (Sr) are also present at short offset. In (a) only, strong bottom reflections are visible (rP), along with low-frequency energetic events (C). In (b) and (d), P and SW propagation modes are confirmed (maxima in black, with 0, 1, 2, and 3 being the SW fundamental and first, second, and third higher modes, respectively). The picked dispersion curves are represented with white error bars.
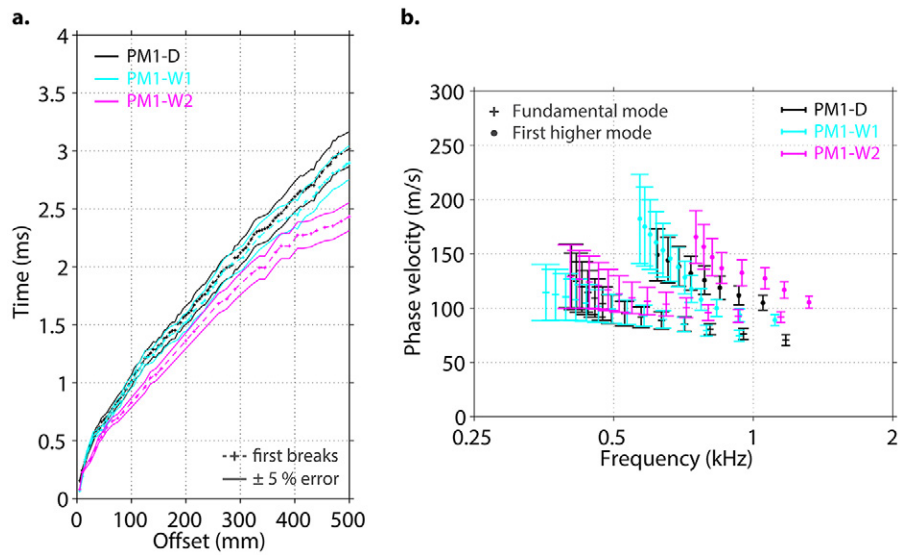

Fig. 6. (a) Pressure (P)-wave first arrival times picked for the dry model PM1-D (black) and the wet models PM1-W1 (cyan) and PM1-W2 (magenta) within a ±5% error (solid line); and (b) dispersion curves of the fundamental (crosses) and first higher (dots) SW propagation modes for the dry model PM1-D (black) and the wet models PM1-W1 (cyan) and PM1-W2 (magenta).

The calculated time differences are represented within their error bars along with the corresponding water and capillary fringe levels in Fig. 7a for PM1-W1 and in Fig. 7b for PM1-W2. For both models, they provide information for depths between 0 and 125 mm. Time differences calculated for PM1-W1 remain mostly under 0.05 ms above z_{cap}, then become slightly more pronounced. However, the limited investigation depth and the large uncertainties prevent imaging a significant trend of the time difference curve. In comparison, time differences calculated for PM1-W2 are significantly greater than the uncertainties, even at shallow depth. The most striking feature is the good consistency between the two inflection points of the time difference curve with both z_{cap} and z_{wat}. For their part, phase velocity differences are represented within their error bars along with the corresponding water and capillary fringe levels in Fig. 7c for PM1-W1 and in Fig. 7d for PM1-W2. They provide deeper information, going from 50 to 200 mm in depth, with larger uncertainties. For PM1-W1, phase velocity differences mainly range within ± 2 m s^{-1} and show a decreasing trend below z_{wat}. This trend, however, remains challenging to interpret given the large uncertainties associated with these data. As for PM1-W2, the calculated phase velocity differences observed between z_{cap} and z_{wat} show a significant increase in the phase velocity, while the large uncertainties at larger depth prevent a comprehensive interpretation.

◦ Discussion and Conclusions

In this study, we focused on the use of seismic methods for monitoring the thicknesses of the fully, partially, and unsaturated areas in the near surface. They were proposed to complement the widely used geoelectric and electromagnetic methods. Indeed, seismic prospecting techniques allow the characterization of the mechanical properties of the probed medium, which are themselves directly influenced by the presence of water.

Following the methodology proposed by Jacob et al. (2008) and Bodet et al. (2010, 2014), we performed laser-Doppler experiments on unconsolidated granular media presenting different water levels. We successfully adapted the laboratory setup developed by Bodet et al. (2010, 2014) to keep the size and weight of the entire setup to a practical level while meeting experimental requirements in terms of boundary wall impermeability and rigidity. Using a laser-Doppler vibrometer and a mechanical source, we recorded small-scale seismograms at the surface of a granular medium made of GBs. Despite sensible noise in the data due to the reduced dimensions of the setup, we were able to extract reliable P-wave travel time and SW dispersion data for the dry and wet models by muting the obtained seismograms. After validating the travel times and phase velocities obtained for the dry granular medium with elastic three-dimensional finite difference simulations, we inverted these data to infer one-dimensional V_P and V_S profiles following a power-law trend with depth, as suggested by theoretical models. Retrieved coefficients were close to 1/3, as previously observed by Jacob et al. (2008) and Bodet et al. (2010, 2014).

The water level was then increased stepwise in the granular medium so as to obtain two distinct wet models with different water levels. For both models, we visually estimated the thickness of the capillary fringe through the glass walls of the experimental tank. When increasing the water level, it unexpectedly appeared that the thickness of the capillary fringe was decreasing, with a difference of around 10 mm between the two wet models. In this study, the mechanical characterization of dry GB models was performed
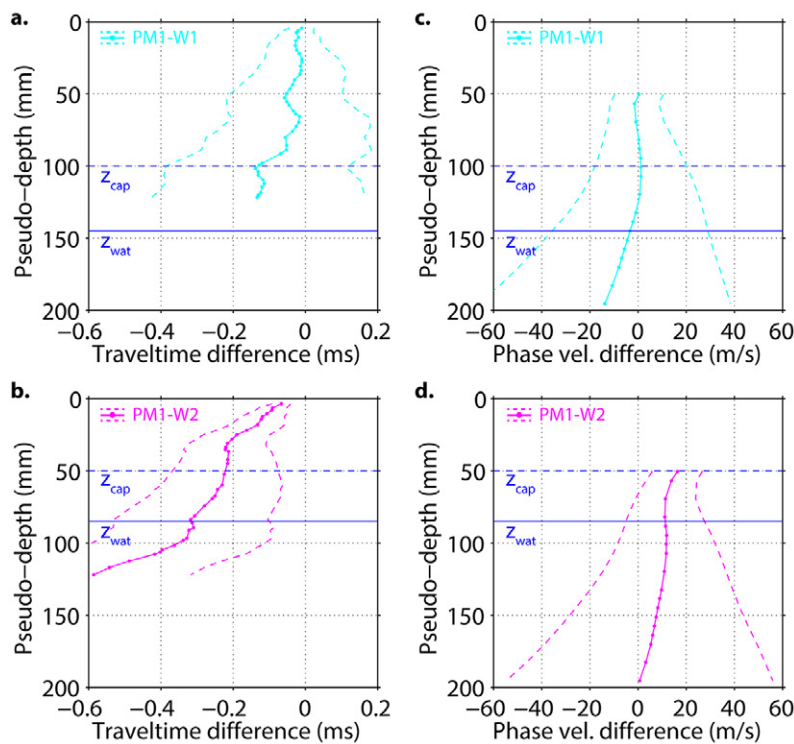

Fig. 7. Travel-time differences and their corresponding error bars calculated between experimental first arrival times obtained for the reference dry model PM1-D and those obtained for the wet models (a) PM1-W1 and (b) PM1-W2 and phase velocity differences and their corresponding error bars calculated between experimental dispersion curves of the fundamental mode obtained for the reference dry model PM1-D and those obtained for the wet models (c) PM1-W1 and (d) PM1-W2. The corresponding water level z_{wat} and capillary fringe depth z_{cap} are represented for both models with blue solid and dashed lines, respectively.

assuming a negligible contribution of density variation to velocity changes in comparison with the contribution of the medium moduli variations (Gusev et al., 2006; Aleshin et al., 2007). However, the density profile of GB models might not be completely constant with depth. Actually, GBs located at the very near surface might be at pressures <100 Pa and present a lower volume fraction. These small volume variations probably lead to significant changes in the pore size distribution, with a non-negligible influence on capillary forces and therefore on water retention properties, thus explaining the thinner capillary fringe observed in PM1-W2.

Despite those disparities, the data extracted from the wet models clearly showed the influence of the increasing water level on the recorded wave field. Yet, if the estimation of the elastic parameters of the dry medium can now be achieved in a relatively straightforward manner in the framework of elastic wave propagation in stratified media, it remains difficult to invert the data obtained for partially saturated granular media in the absence of a comprehensive theoretical model. To overcome these drawbacks, we studied the differences in travel time and phase velocity observed between the dry and wet models.

For PM1-W1, the differences were mostly insignificant due to a limited investigation depth and large uncertainties in the data. For P-wave travel times, water content changes occurred at a depth close to the maximum depth of investigation (around 125 mm), while the changes induced on SW phase velocities were too small to be accurately detected in the range of errors. In comparison, the results obtained for PM1-W2 show significant differences, especially regarding P-wave travel times. The travel-time difference curve indeed presents two inflection points that closely match both water and capillary fringe levels. The highest travel-time difference (i.e., the highest P-wave velocity increase) happens in the fully saturated area, while an intermediate increase takes place in the partially saturated area. An unsettling feature is the travel-time difference observed in the supposedly dry area, which we believe is due to residual humidity that reached the top of the granular medium. The amount of such humidity is probably too small to be seen with the naked eye but still sufficient to increase the rigidity of the medium. As for phase velocity differences, they do not provide information at greater depth due to large uncertainties at low frequencies. They present a significant phase velocity increase in the capillary fringe, however, which can be explained by the creation of "liquid bridges" between the beads, as observed by Bocquet et al. (1998), Soulié (2005), or Vandewalle et al. (2012). These "liquid bridges" might be able to increase the rigidity of the medium (and thus the velocity) compared with a fully air- or water-saturated medium where lower phase velocities are expected.

This simple tool provided satisfactory results for the highest water level, which are interestingly consistent with the observed water level and depth of the capillary fringe. It also offers attractive prospects for studying soil water content variations in the field in a qualitative manner, keeping in mind the limitations imposed by the spread length

and the lateral variability of a real environment in terms of resolution and depth of investigation. Be that as it may, an increasing number of time-lapse seismic studies have been providing promising results regarding the monitoring of significant differences in the seismic data linked to soil water content variations. These studies were performed in real partially saturated environments at various time scales ranging from a few hours (Konishi et al., 2015), to daily tidal cycles (West and Menke, 2000), periods of some months (Jefferson et al., 1998; Pasquet et al., 2015a), and up to full yearly cycles (Lu, 2014; Bergamo et al., 2015, 2016), where the seasonal change in water content related to the temporal distribution of precipitation can be appreciated. In these studies, either laser-Doppler acoustic probing (Lu, 2014) or typical seismic acquisition equipment (Jefferson et al., 1998; West and Menke, 2000; Konishi et al., 2015; Pasquet et al., 2015a; Bergamo et al., 2015, 2016) was used. These studies have shown the good sensitivity of seismic data (phase velocity, travel time, and amplitude) to variations in water content in the vadose zone. The researchers worked in soils with water content variations ranging from 5 to 20% and were able to observe phase velocity differences ranging from ± 10 to 50 m s^{-1}. As of now, this approach has been applied to qualitative time-lapse monitoring of soil water content variations (Bergamo et al., 2016) and quantitative estimation of the water table level (Pasquet et al., 2015a). Along with TDR measurements at the laboratory scale to calibrate seismic data in terms of water content, this methodology will be deployed at the field scale within a multiscale, multi-method approach coupling different geophysical and hydrological parameters on the Orgeval experimental basin (Mouhri et al., 2013) to monitor spatiotemporal surface–subsurface water exchange.

Appendix
Numerical Validation of the Mute

The validity of the estimated V_P and V_S profiles and of our interpretations in terms of water saturation variations in the GBs mainly relies on the accuracy of picking travel-time and dispersion curves. However, the reduced dimensions of the tank caused the appearance of strong backscattered events that masked part of the signal contained in the SW wave train (C in Fig. 8a). Consequently, the dispersion image obtained by transforming the full wave field into the frequency–phase velocity domain presents strong maxima that are hardly distinguishable from each other (Fig. 8b). The application of a mute (blue contour in Fig. 8a) clearly enhanced the quality of the dispersion image and allowed identification of the SW fundamental (0) and first higher (1) propagation modes, along with a faster P mode (Fig. 8c).

If the mute clearly helped in identifying and picking dispersion curves, it also removed a significant part of the wave field whose importance is hard to assess. We propose here to use the elastic parameters estimated after muting with the dry model as inputs to a three-dimensional numerical model of the experiment to compare recorded data to a synthetic wave field computed from an
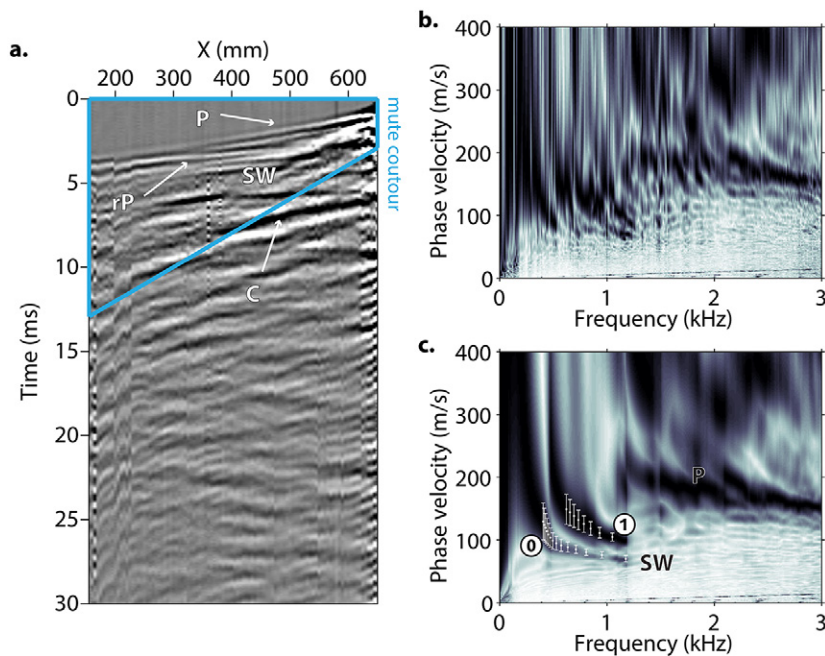
Fig. 8. (a) Seismogram of the vertical component of particle velocity recorded at the surface of the dry model PM1-D—the blue contour corresponds to the limits of the mute applied prior to the extraction of the dispersion image, the recorded wave field presents coherent P and SW events, and strong bottom reflections are visible (rP), along with low-frequency energetic events (C); (b) dispersion image extracted before the mute, where P and SW propagation modes cannot be clearly identified; and (c) dispersion image extracted after the mute, where P and SW propagation modes are confirmed (maxima in black, with 0 and 1 being the SW fundamental and first higher modes, respectively). The picked dispersion curves are represented with white error bars.

elastic finite difference formulation of the problem and address the limits of such a processing technique. For that purpose, we modeled the center part of the tank (without the side reservoirs) and performed two distinct simulations to retrieve synthetic seismograms both with and without reflection and backscattering on the box walls.

Numerical Model

On the one hand, Dirichlet conditions (zero velocities, i.e., total reflection) were imposed on each side of the box. On the other hand, we used absorbing conditions with convolutional perfectly matched layer (CPML), as developed in three-dimensional finite difference formulations for purely elastic, poroelastic, or viscoelastic media (Komatitsch and Martin, 2007; Martin et al., 2008; Martin and Komatitsch, 2009). For Dirichlet and CPML simulations, the bottom of the box was defined with Dirichlet conditions while the free surface at the top of the computational domain was implemented using the zero normal traction assumption. The numerical model (NM1) was discretized by elements of 0.5 by 0.5 by 0.5 mm for a mesh of 1600 by 601 by 511. This led to a model of 0.8 m in length by 0.255 m in depth and by 0.3 m in width. For the second simulation, the mesh was extended by CPML layers discretized over 10 points on each side of the box (the effective width including the CPML had a size of 0.31 m). The simulated model was laterally homogeneous and its velocities followed the power-law trend with depth defined above, with the parameters estimated experimentally and summarized in Fig. 4 ($\gamma_P = 21.25$, $\alpha_P = 0.33$, $\gamma_S = 13.10$, $\alpha_S = 0.297$).

According to the discretization, velocities varied from $V_P = 42$ m s^{-1} and $V_S = 24$ m s^{-1} close to the free surface up to $V_P = 329$ m s^{-1} and $V_S = 154$ m s^{-1} at the bottom (the bulk density being 1600 kg m^{-3} as observed in the experiments). The time step $\Delta t = 0.4$ µs corresponded to a stability Courant–Friedrichs–Lewy number of 0.3. The grid spacing corresponded to nearly seven points discretization per minimum wavelength, which was well taken into account by our fourth-order staggered finite difference spatial discretization. The source has been carefully implemented to match, as far as possible, the experimental conditions described in Fig. 2. The geometry of the buried part of the stick has been projected onto the numerical mesh, and we implemented the experimental force source signal. The source was thus located at 0.15 m from the right side of the box. The receivers were spaced every 5 mm (10 grid points) all along the length of the model at the free surface. To be able to reduce the computational time, we ran the simulations over 160 Intel Xeon processors of the CALMIP computing center located in Toulouse (France) or the TGCC-Curie machine at GENCI in Paris. The box was cut in slices along the largest dimension (O_x length direction), and information between processors was sent by using hybrid openMP/'send-receive' MPI communications.

Numerical Results and Comparisons with Experimental Data

The seismogram obtained for the first simulation performed with Dirichlet conditions (NM1-DIR) is represented in Fig. 9a and shows events corresponding to those identified in PM1-D, namely the P-wave first arrivals (P), the surface-wave wave field (SW), the bottom reflections (rP), and the backscattered and converted waves (C). As observed for PM1-D, the dispersion image extracted from the full seismogram (Fig. 9b) is corrupted by a high level of noise, and none of the P or SW events can be identified. After applying the same mute used for PM1-D to the NM1-DIR seismogram (blue contour in Fig. 9a), we extracted a dispersion image in which SW events can be clearly identified

(Fig. 9c). These events and those observed on the PM1-D dispersion image (Fig. 8c) have a similar velocity range, with higher frequencies for the results of numerical modeling.

The seismogram obtained for the second simulation (Fig. 10a) with absorbing conditions on the four sides of the box (NM1-CPML) presents only some of the events observed in PM1-D. The P-wave first arrivals (P), the surface-wave wave field (SW), and the bottom reflections (rP) are clearly identified, but the high-energy and low-frequency events previously identified are obviously missing, confirming that these events originated from the conversion and backscattering of guided waves at the interface between the granular medium and the glass walls of the tank. The dispersion image extracted from the full seismogram directly presents

well-defined SW propagation modes (Fig. 10b). In comparison, the dispersion image obtained after applying the same mute used for PM1-D to the NM1-CPML seismogram (blue contour in Fig. 10a) shows the same maxima but helps in the identification of the first higher mode (Fig. 10c).

The first-arrival time of the numerical data was picked at each trace for both simulated seismograms and compared with the theoretical and experimental travel time vs. offset curve (Fig. 11a). Numerical arrival times clearly fit experimental and theoretical results within a ±5% error, confirming the negligible influence of reflection and backscattering events on P-wave first arrival times. As for dispersion curves picked for the SW modes identified on the dispersion images (Fig. 11b), they also fit experimental and
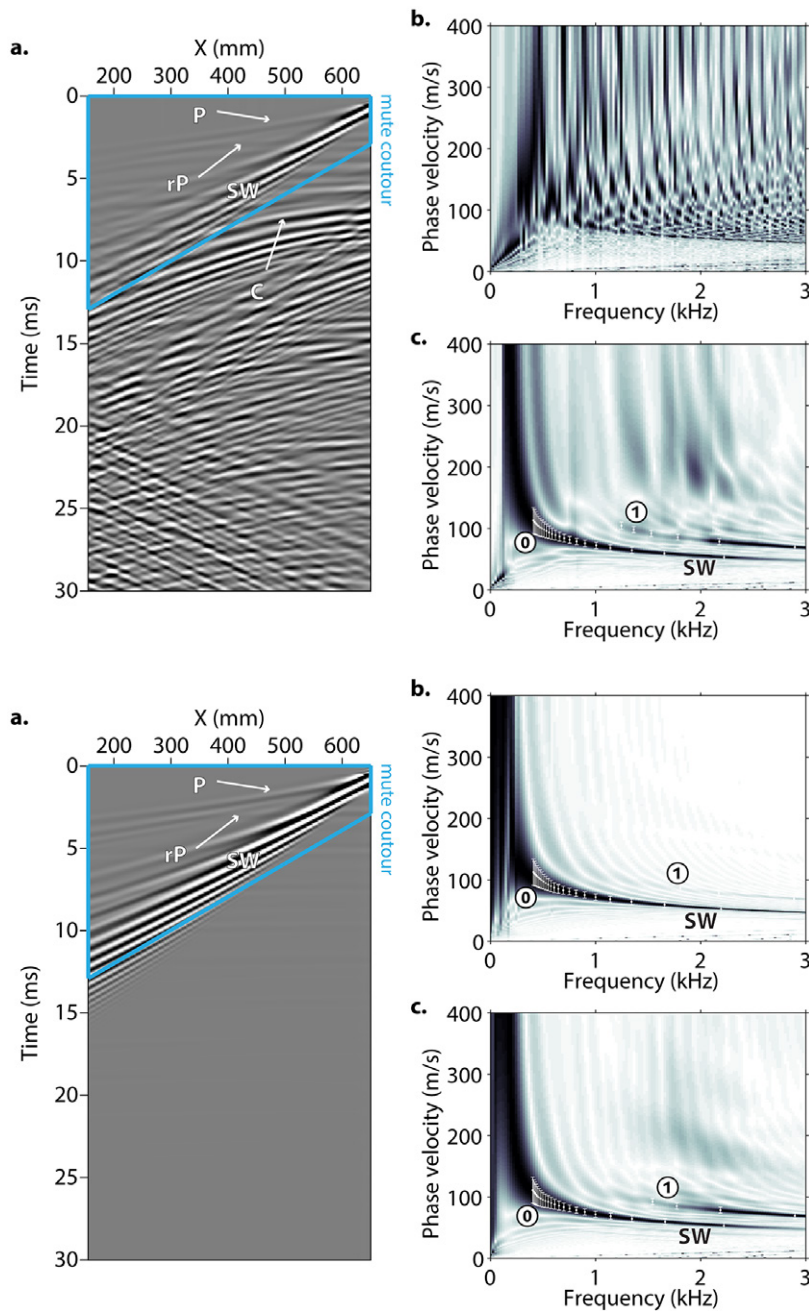

Fig. 9. (a) Seismogram of the vertical component of particle velocity computed at the free surface of the numerical model NM1-DIR—the blue contour corresponds to the limits of the mute applied prior to the extraction of the dispersion image, the recorded wave field presents coherent P and SW events, and strong bottom reflections are visible (rP), along with low-frequency energetic events (C); (b) dispersion image extracted before the mute, where P and SW propagation modes cannot be clearly identified; and (c) dispersion image extracted after the mute, where P and SW propagation modes are confirmed (maxima in black, with 0 and 1 being the SW fundamental and first higher modes, respectively). The picked dispersion curves are represented with white error bars.

Fig. 10. (a) Seismogram of the vertical component of particle velocity computed at the free surface of the numerical model NM1-CPML—the blue contour corresponds to the limits of the mute applied prior to the extraction of the dispersion image, and the recorded wave field presents coherent P and SW events, along with strong bottom reflections (rP); (b) dispersion image extracted before the mute; and (c) dispersion image extracted after the mute. In (b) and (c), P and SW propagation modes are confirmed (maxima in black, with 0 and 1 being the SW fundamental and first higher modes, respectively). The picked dispersion curves are represented with white error bars.
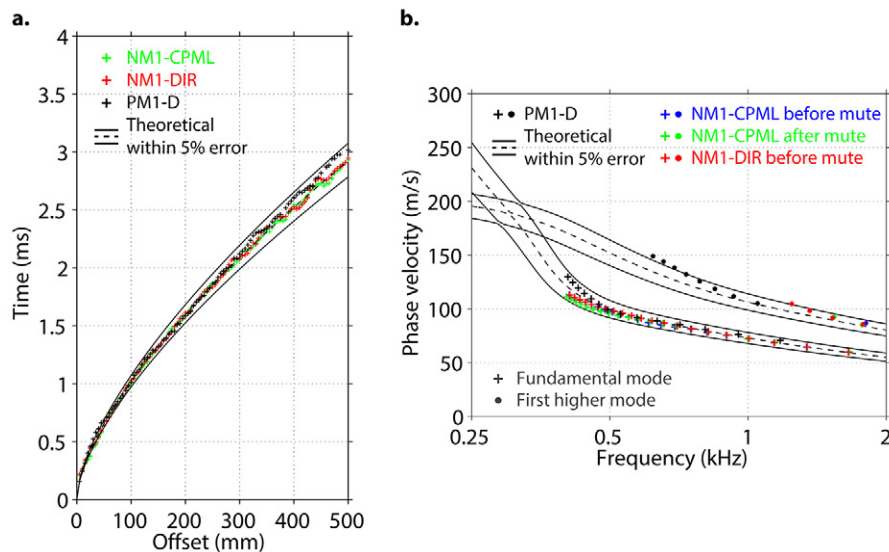
Fig. 11. (a) Pressure (P)-wave first arrivals picked for the numerical models NM1-CPML (green crosses) and NM1-DIR (red crosses) and the dry model PM1-D (black crosses), with theoretical travel times computed from the elastic parameters estimated in PM1-D represented in black (dashed line) within a ±5% error (solid line); and (b) dispersion curves of the fundamental (crosses) and first (dots) higher SW propagation modes obtained for NM1-CPML before mute (blue), NM1-CPML after mute (green), NM1-DIR after mute (red), and PM1-D (black), with theoretical dispersion curves computed from the elastic parameters estimated in PM1-D represented in black (dashed line) within a ±5% error (solid line).

theoretical dispersion within a ±5% error, with yet a slight velocity shift at low frequency. Nevertheless, these results validate the dispersion curves extracted after the mute and confirm the soundness of the muting approach for retrieving dispersion data in the presence of strong backscattering and reflection events.

Acknowledgments

References

Abraham, O., B. Piwakowski, G. Villain, and O. Durand. 2012. Non-contact, automated surface wave measurements for the mechanical characterisation of concrete. Construct. Build. Mater. 37:904–915. doi:10.1016/j.conbuildmat.2012.03.015

Aleshin, V., V. Gusev, and V. Tournat. 2007. Acoustic modes propagating along the free surface of granular media. J. Acoust. Soc. Am. 121:2600–2611. doi:10.1121/1.2714923

Amidu, S.A., and J.A. Dunbar. 2007. Geoelectric studies of seasonal wetting and drying of a Texas Vertisol. Vadose Zone J. 6:511–523. doi:10.2136/vzj2007.0005

Bachrach, R., J. Dvorkin, and A. Nur. 1998. High-resolution shallow-seismic experiments in sand: II. Velocities in shallow unconsolidated sand. Geophysics 63:1234–1240. doi:10.1190/1.1444424

Bachrach, R., J. Dvorkin, and A. Nur. 2000. Seismic velocities and Poisson's ratio of shallow unconsolidated sands. Geophysics 65:559–564. doi:10.1190/1.1444751

Bachrach, R., and A. Nur. 1998. High-resolution shallow-seismic experiments in sand: I. Water table, fluid flow, and saturation. Geophysics 63:1225–1233. doi:10.1190/1.1444423

Bear, J. 1972. Dynamics of fluids in porous media. Elsevier, New York.

Bechkit, M.A., S. Flageul, R. Guerin, and A. Tabbagh. 2014. Monitoring soil water content by vertical temperature variations. Ground Water 52:566–572. doi:10.1111/gwat.12090

Bergamo, P., L. Bodet, L.V. Socco, R. Mourgues, and V. Tournat. 2014. Physical modelling of a surface-wave survey over a laterally varying granular medium with property contrasts and velocity gradients. Geophys. J. Int. 197:233–247. doi:10.1093/gji/ggt521

Bergamo, P., B. Dashwood, S. Uhlemann, R. Swift, J.E. Chambers, D.A. Gunn, and S. Donohue. 2016. Time-lapse monitoring of climate effects on earthworks using surface waves. Geophysics 81:EN1–EN15. doi:10.1190/geo2015-0275.1

Bergamo, P., S. Donohue, D.A. Gunn, B. Dashwood, S. Uhlemann, J.E. Chambers, and D. Ward. 2015. Time-lapse monitoring of the slopes of a heritage earthwork by means of near-surface seismic techniques. In: Near Surface Geosciences 2015: 21st European Meeting of Environmental and Engineering Geophysics, Turin, Italy. 6–10 Sept. 2015. Eur. Assoc. Geosci. Eng., Houten, the Netherlands. p. 266–270. doi:10.3997/2214-4609.201413717

Binley, A., S.S. Hubbard, J.A. Huisman, A. Revil, D.A. Robinson, K. Singha, and L.D. Slater. 2015. The emergence of hydrogeophysics for improved understanding of subsurface processes over multiple scales. Water Resour. Res. 51:3837–3866. doi:10.1002/2015WR017016

Biot, M.A. 1956a. Theory of propagation of elastic waves in a fluid-saturated porous solid: I. Low-frequency range. J. Acoust. Soc. Am. 28:168–178. doi:10.1121/1.1908239

Biot, M.A. 1956b. Theory of propagation of elastic waves in a fluid-saturated porous solid: II. Higher frequency range. J. Acoust. Soc. Am. 28:179–191. doi:10.1121/1.1908241

Bishop, A.W. 1959. The principle of effective stress. Tek. Ukebl. 106:859–863.

Bocquet, L., E. Charlaix, S. Ciliberto, and J. Crassous. 1998. Moisture-induced ageing in granular media and the kinetics of capillary condensation. Nature 396:735–737. doi:10.1038/25492

Bodet, L., O. Abraham, and D. Clorennec. 2009. Near-offset effects on Rayleigh-wave dispersion measurements: Physical modeling. J. Appl. Geophys. 68:95–103. doi:10.1016/j.jappgeo.2009.02.012

Bodet, L., A. Dhemaied, R. Martin, R. Mourgues, F. Rejiba, and V. Tournat. 2014. Small-scale physical modeling of seismic-wave propagation using unconsolidated granular media. Geophysics 79:T323–T339. doi:10.1190/geo2014-0129.1

Bodet, L., A. Dhemaied, R. Mourgues, V. Tournat, and F. Rejiba. 2012. Laser-Doppler acoustic probing of granular media with in-depth property gradient and varying pore pressures. AIP Conf. Proc. 1433:147. doi:10.1063/1.3703158

Bodet, L., X. Jacob, V. Tournat, R. Mourgues, and V.E. Gusev. 2010. Elasticity profile of an unconsolidated granular medium inferred from guided waves: Toward acoustic monitoring of analogue models. Tectonophysics 496:99–104. doi:10.1016/j.tecto.2010.10.004

Bodet, L., K. van Wijk, A. Bitri, O. Abraham, P. Côte, G. Grandjean, and D. Leparoux. 2005. Surface-wave inversion limitations from laser-Doppler physical modeling. J. Environ. Eng. Geophys. 10:151–162. doi:10.2113/JEEG10.2.151

Bonneau, L., B. Andreotti, and E. Clément. 2008. Evidence of Rayleigh–Hertz surface waves and shear stiffness anomaly in granular media. Phys. Rev. Lett. 101:118001. doi:10.1103/PhysRevLett.101.118001

Bretaudeau, F., D. Leparoux, O. Durand, and O. Abraham. 2011. Small-scale modeling of onshore seismic experiment: A tool to validate numerical modeling and seismic imaging methods. Geophysics 76:T101–T112. doi:10.1190/geo2010-0339.1

Brunet, T., X. Jia, and P. Mills. 2008. Mechanisms for acoustic absorption in dry and weakly wet granular media. Phys. Rev. Lett. 101:138001. doi:10.1103/PhysRevLett.101.138001

de Cacqueray, B., P. Roux, M. Campillo, and S. Catheline. 2013. Tracking of velocity variations at depth in the presence of surface velocity fluctuations. Geophysics 78:U1–U8. doi:10.1190/geo2012-0071.1

de Cacqueray, B., P. Roux, M. Campillo, S. Catheline, and P. Boue. 2011. Elastic-wave identification and extraction through array processing: An experimental investigation at the laboratory scale. J. Appl. Geophys. 74:81–88. doi:10.1016/j.jappgeo.2011.04.005

Campman, X., K. van Wijk, C.D. Riyanti, J.A. Scales, and G. Herman. 2004. Imaging scattered seismic surface waves. Near Surf. Geophys. 2:223–230.

Campman, X., K. van Wijk, J.A. Scales, and G. Herman. 2005. Imaging and suppressing near-receiver scattered surface waves. Geophysics 70:V21–V29. doi:10.1190/1.1884831

Cassiani, G., N. Ursino, R. Deiana, G. Vignoli, J. Boaga, M. Rossi, et al. 2012. Noninvasive monitoring of soil static characteristics and dynamic states: A case study highlighting vegetation effects on agricultural land. Vadose Zone J. 11(3). doi:10.2136/vzj2011.0195

Cheviron, B., R. Guérin, A. Tabbagh, and H. Bendjoudi. 2005. Determining long-term effective groundwater recharge by analyzing vertical soil temperature profiles at meteorological stations. Water Resour. Res. 41:W09501. doi:10.1029/2005WR004174

Cho, G.C., and J.C. Santamarina. 2001. Unsaturated particulate materials: Particle-level studies. J. Geotech. Geoenviron. Eng. 127:84–96. doi:10.1061/(ASCE)1090-0241(2001)127:1(84)

Fredlund, D.G., N.R. Morgenstern, and R.A. Widger. 1978. The shear strength of unsaturated soils. Can. Geotech. J. 15:313–321. doi:10.1139/t78-029

Fredlund, D.G., and H. Rahardjo. 1993. Soil mechanics for unsaturated soils. John Wiley & Sons, Hoboken, NJ. doi:10.1002/9780470172759

Garré, S., I. Coteur, C. Wongleecharoen, T. Kongkaew, J. Diels, and J. Vanderborght. 2013. Noninvasive monitoring of soil water dynamics in mixed cropping systems: A case study in Ratchaburi province, Thailand. Vadose Zone J. 12(2). doi:10.2136/vzj2012.0129

Garré, S., M. Javaux, J. Vanderborght, L. Pagès, and H. Vereecken. 2011. Three-dimensional electrical resistivity tomography to monitor root zone water dynamics. Vadose Zone J. 10:412–424. doi:10.2136/vzj2010.0079

Gassmann, F. 1951. Elastic waves through a packing of spheres. Geophysics 16:673–685. doi:10.1190/1.1437718

Gusev, V., V. Aleshin, and V. Tournat. 2006. Acoustic waves in an elastic channel near the free surface of granular media. Phys. Rev. Lett. 96:214301. doi:10.1103/PhysRevLett.96.214301

Huisman, J.A., S.S. Hubbard, J.D. Redman, and A.P. Annan. 2003. Measuring soil water content with ground penetrating radar. Vadose Zone J. 2:476–491. doi:10.2136/vzj2003.4760

Ines, A.V.M., and B.P. Mohanty. 2008. Near-surface soil moisture assimilation for quantifying effective soil hydraulic properties using genetic algorithms: 1. Conceptual modeling. Water Resour. Res. 44:W06422.

Ines, A.V.M., and B.P. Mohanty. 2009. Near-surface soil moisture assimilation for quantifying effective soil hydraulic properties using genetic algorithms: 2. Using airborne remote sensing during SGP97 and SMEX02. Water Resour. Res. 45:W01408.

Jacob, X., V. Aleshin, V. Tournat, P. Leclaire, W. Lauriks, and V.E. Gusev. 2008. Acoustic probing of the jamming transition in an unconsolidated granular medium. Phys. Rev. Lett. 100:158003. doi:10.1103/PhysRevLett.100.158003

Jefferson, R.D., D.W. Steeples, R.A. Black, and T. Carr. 1998. Effect of soil-moisture content on shallow-seismic data. Geophysics 63:1357–1362. doi:10.1190/1.1444437

Komatitsch, D., and R. Martin. 2007. An unsplit convolutional perfectly matched layer improved at grazing incidence for the seismic wave equation. Geophysics 72:SM155–SM167. doi:10.1190/1.2757586

Konishi, C., T. Ishizawa, T. Danjo, and N. Sakai. 2015. S-wave velocity monitoring during an artificial rainfall experiment using large scale rainfall simulator. In: Near Surface Geosciences 2015: 21st European Meeting of Environmental and Engineering Geophysics, Turin, Italy. 6–10 Sept. 2015. Eur. Assoc. Geosci. Eng., Houten, the Netherlands. p. 135–139.

Konstantaki, L.A., S.F.A. Carpentier, F. Garofalo, P. Bergamo, and L.V. Socco. 2013. Determining hydrological and soil mechanical parameters from multichannel surface-wave analysis across the Alpine Fault at Inchbonnie, New Zealand. Near Surf. Geophys. 11:435–448.

Lu, L., M. Chekroun, O. Abraham, V. Maupin, and G. Villain. 2011. Mechanical properties estimation of functionally graded materials using surface waves recorded with a laser interferometer. NDT Int. 44:169–177. doi:10.1016/j.ndteint.2010.11.007

Lu, N., and W.J. Likos. 2004. Unsaturated soil mechanics. John Wiley & Sons, Hoboken, NJ.

Lu, Z. 2014. Feasibility of using a seismic surface wave method to study seasonal and weather effects on shallow surface soils. J. Environ. Eng. Geophys. 19:71–85. doi:10.2113/JEEG19.2.71

Maillot, B. 2013. A sedimentation device to produce uniform sand packs. Tectonophysics 593:85–94. doi:10.1016/j.tecto.2013.02.028

Makse, H.A., N. Gland, D.L. Johnson, and L. Schwartz. 2004. Granular packings: Nonlinear elasticity, sound propagation, and collective relaxation dynamics. Phys. Rev. E 70:061302. doi:10.1103/PhysRevE.70.061302

Martin, R., and D. Komatitsch. 2009. An unsplit convolutional perfectly matched layer technique improved at grazing incidence for the viscoelastic wave equation. Geophys. J. Int. 179:333–344. doi:10.1111/j.1365-246X.2009.04278.x

Martin, R., D. Komatitsch, and A. Ezziani. 2008. An unsplit convolutional perfectly matched layer improved at grazing incidence for seismic wave propagation in poroelastic media. Geophysics 73:T51–T61. doi:10.1190/1.2939484

Martini, E., U. Wollschläger, S. Kögler, T. Behrens, P. Dietrich, F. Reinstorf, et al. 2015. Spatial and temporal dynamics of hillslope-scale soil moisture patterns: Characteristic states and transition mechanisms. Vadose Zone J. 14(4). doi:10.2136/vzj2014.10.0150

Mokhtar, T.A., R.B. Herrmann, and D.R. Russell. 1988. Seismic velocity and Q model for the shallow structure of the Arabian Shield from short-period Rayleigh waves. Geophysics 53:1379–1387. doi:10.1190/1.1442417

Mouhri, A., N. Flipo, F. Rejiba, C. de Fouquet, L. Bodet, B. Kurtulus, et al. 2013. Designing a multi-scale sampling system of stream–aquifer interfaces in a sedimentary basin. J. Hydrol. 504:194–206. doi:10.1016/j.jhydrol.2013.09.036

Murillo, C., L. Thorel, and B. Caicedo. 2009. Ground vibration isolation with geofoam barriers: Centrifuge modeling. Geotextiles Geomembranes 27:423–434. doi:10.1016/j.geotexmem.2009.03.006

Nishizawa, O., T. Satoh, X. Lei, and Y. Kuwahara. 1997. Laboratory studies of seismic wave propagation in inhomogeneous media using a laser Doppler vibrometer. Bull. Seismol. Soc. Am. 87:809–823.

Njoku, E.G., and D. Entekhabi. 1996. Passive microwave remote sensing of soil moisture. J. Hydrol. 184:101–129. doi:10.1016/0022-1694(95)02970-2

O'Neill, A. 2003. Full-waveform reflectivity for modelling, inversion and appraisal of seismic surface wave dispersion in shallow site investigations. Ph.D. diss. Univ. of Western Australia, Perth, WA, Australia.

Parsekian, A.D., K. Singha, B.J. Minsley, W.S. Holbrook, and L. Slater. 2015. Multiscale geophysical imaging of the critical zone. Rev. Geophys. 53:1–26. doi:10.1002/2014RG000465

Pasquet, S., L. Bodet, A. Dhemaied, A. Mouhri, Q. Vitale, F. Rejiba, et al. 2015a. Detecting different water table levels in a shallow aquifer with combined P-, surface and SH-wave surveys: Insights from V_P/V_S or Poisson's ratios. J. Appl. Geophys. 113:38–50. doi:10.1016/j.jappgeo.2014.12.005

Pasquet, S., L. Bodet, L. Longuevergne, A. Dhemaied, C. Camerlynck, F. Rejiba, and R. Guérin. 2015b. 2D characterization of near-surface V_P/V_S: Surface-wave dispersion inversion versus refraction tomography. Near Surf. Geophys. 13:315–331.

Read, T., O. Bour, V. Bense, T. Le Borgne, P. Goderniaux, M. Klepikova, et al. 2013. Characterizing groundwater flow and heat transport in fractured rock using fiber-optic distributed temperature sensing. Geophys. Res. Lett. 40:2055–2059. doi:10.1002/grl.50397

Reedy, R.C., and B.R. Scanlon. 2003. Soil water content monitoring using electromagnetic induction. J. Geotech. Geoenviron. Eng. 129:1028–1039. doi:10.1061/(ASCE)1090-0241(2003)129:11(1028)

Robinson, D.A., C.S. Campbell, J.W. Hopmans, B.K. Hornbuckle, S.B. Jones, R. Knight, et al. 2008. Soil moisture measurement for ecological and hydrological watershed-scale observatories: A review. Vadose Zone J. 7:358–389. doi:10.2136/vzj2007.0143

Robinson, D.A., S.B. Jones, J.M. Wraith, D. Or, and S.P. Friedman. 2003. A review of advances in dielectric and electrical conductivity measurement in soils using time domain reflectometry. Vadose Zone J. 2:444–475. doi:10.2136/vzj2003.4440

Ruiz, A., and P.B. Nagy. 2004. Laser-ultrasonic surface wave dispersion measurements on surface-treated metals. Ultrasonics 42:665–669. doi:10.1016/j.ultras.2004.01.045

Russel, D.R. 1987. Multi-channel processing of dispersed surface waves. Ph.D. diss. Saint Louis Univ., Saint Louis, MO.

Soulié, F. 2005. Cohésion par capillarité et comportement mécanique de milieux granulaires. Ph.D. diss. Univ. Montpellier II, Montpellier, France.

Takagi, K., and H. Lin. 2011. Temporal dynamics of soil moisture spatial variability in the Shale Hills Critical Zone Observatory. Vadose Zone J. 10:832–842. doi:10.2136/vzj2010.0134

Terzaghi, K. 1936. The shearing resistance of saturated soils and the angle between the planes of shear. In: Proceedings of the 1st International Conference on Soil Mechanics and Foundation Engineering, Cambridge, MA. Harvard Print. Office, Cambridge, MA. p. 54–56.

Toker, N.K., J.T. Germaine, and P.J. Culligan. 2014. Effective stress and shear strength of moist uniform spheres. Vadose Zone J. 13(5). doi:10.2136/vzj2013.07.0129

Topp, G.C., J.L. Davis, and A.P. Annan. 1980. Electromagnetic determination of soil water content: Measurements in coaxial transmission lines. Water Resour. Res. 16:574–582. doi:10.1029/WR016i003p00574

Topp, G.C., M. Yanuka, W.D. Zebchuk, and S. Zegelin. 1988. Determination of electrical conductivity using time domain reflectometry: Soil and water experiments in coaxial lines. Water Resour. Res. 24:945–952. doi:10.1029/WR024i007p00945

Tournat, V., and V.E. Gusev. 2010. Acoustics of unconsolidated "model" granular media: An overview of recent results and several open problems. Acta Acust. United Acust. 96:208–224. doi:10.3813/AAA.918271

Vandewalle, N., G. Lumay, F. Ludewig, and J.E. Fiscina. 2012. How relative humidity affects random packing experiments. Phys. Rev. E 85:031309. doi:10.1103/PhysRevE.85.031309

van Wijk, K., and A.L. Levshin. 2004. Surface wave dispersion from small vertical scatterers. Geophys. Res. Lett. 31:L20602. doi:10.1029/2004GL021007

Vereecken, H., L. Weihermüller, F. Jonard, and C. Montzka. 2012. Characterization of crop canopies and water stress related phenomena using microwave remote sensing methods: A review. Vadose Zone J. 11(2). doi:10.2136/vzj2011.0138ra

West, M., and W. Menke. 2000. Fluid-induced changes in shear velocity from surface waves. In: 13th EEGS Symposium on the Application of Geophysics to Engineering and Environmental Problems, Arlington, VA. 20–24 Feb. 2000. Environ. Eng. Geophys. Soc., Denver, CO. p. 21–28. doi:10.4133/1.2922747

Xia, J., R.D. Miller, and C.B. Park. 1999. Estimation of near-surface shear-wave velocity by inversion of Rayleigh waves. Geophysics 64:691–700. doi:10.1190/1.1444578

Zimmer, M., M. Prasad, G. Mavko, and A. Nur. 2007. Seismic velocities of unconsolidated sands: 1. Pressure trends from 0.1 to 20 MPa. Geophysics 72:E1–E13. doi:10.1190/1.2399459